H2020 FETOPEN: OPTO SILICON 964191

This project has received funding from the European Union's Horizon 2020 research and innovation programme under grant agreement No 964191.

D 4.4 Carrier dynamics in strained quantum wells

Type of this document	Report
Dissemination level	Public
Date	October 27, 2023
WP	WP4 Strained quantum well (QW) laser on silicon
Authors	Mette Schouten, Marvin van Tilburg, Jos Haverkort
Status	Approved by the whole consortium

This deliverable reflects only the author's view and the Commission is not responsible for any use that may be made of the information it contains.

Carrier cooling dynamics in hex-SiGe

1. Introduction

For integration into silicon photonics, a group IV laser consisting of either strained Ge[1], GeSn[2–8] or hex-SiGe[9] would be a logical choice. One of the fundamental differences between group IV lasers and their group III/V counterparts is however the absence of efficient carrier cooling by optical phonon emission due to the Fröhlich interaction in nonpolar group IV semiconductors[10–12], as illustrated in Fig. 1. The Fröhlich interaction is present in a polar lattice since lattice vibrations give rise to periodically oscillating charges which give rise to potential fields that interact with the photoexcited hot carriers.

.

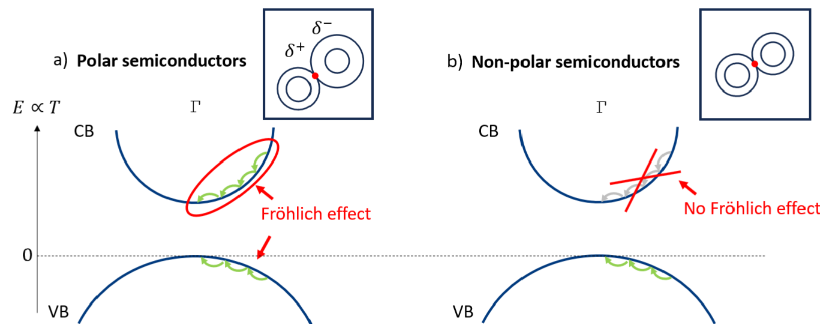

Figure 1: Schematic representation of the difference in hot carrier cooling in polar and non-polar materials. In polar materials (a), the Fröhlich effect is the dominant cooling mechanism, inducing carrier-phonon scattering. In non-polar materials (b), the Fröhlich interaction is not present. Nonpolar deformation potential scattering is taking over as the dominant scattering mechanism, which, however, is not allowed in the s-type Γ-valley of the conduction band.

In nonpolar semiconductors like cubic Ge, deformation potential scattering takes over as the dominant intravalley hot carrier cooling mechanism[13–17]. This scattering process, however, is predicted to be symmetry forbidden in an s-type Γ-valley[18] in the conduction band. The reduction of carrier cooling could have major implications for the lasing application of direct-band gap Group IV semiconductors.

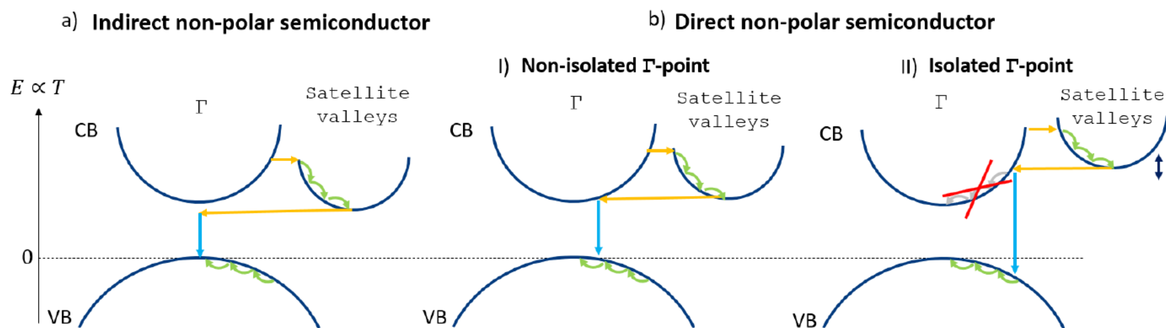

Figure 2: Schematic representation of hot-carrier cooling in nonpolar semiconductors. A distinction is made between indirect bandgap semiconductors (a) such as Si or Ge, and direct bandgap (b) nonpolar semiconductors which are further subdivided into nonpolar semiconductors with a non-isolated Γ-valley such as strained cubic Ge and GeSn (with a not too high Sn composition) (I) and (II) nonpolar semiconductors with an isolated Γ-valley, which is the case for hex-SiGe.

It is important to understand the peculiarities of carrier cooling in hex-SiGe as compared to other more well-known nonpolar semiconductors. In indirect non-polar semiconductors such as e.g. cubic Ge, carrier cooling is dominated by $\Gamma \rightarrow L$ and $L \rightarrow L$ inter-valley deformation potential scattering as well as by intravalley deformation potential scattering in the satellite L-valleys as shown in Fig. 2a. Similar

behavior is observed in direct non-polar semiconductors with a non-isolated Γ-valley as shown in panel (I) of Fig. 2b. In a truly direct bandgap group IV semiconductor like hex-SiGe, which has indirect minima at the M-point or the U-point in reciprocal space[19] (see Table I below), ultrafast carrier cooling will start with $\Gamma \rightarrow M, \Gamma \rightarrow U$ and $M \rightarrow M, U \rightarrow M$ and $U \rightarrow U$ intervalley scattering, possibly followed by intravalley deformation potential scattering in the indirect M-valley and U-valley. These processes are expected at a time scale below 100 femtosecond. In hex-SiGe, the much slower final cooling of electrons to the bottom of the conduction band should now take place in the Γ-valley.
Carrier relaxation in an isolated Γ-valley in a nonpolar semiconductor has not been studied before and is a novel aspect of this report. There are 3 different mechanisms that might be responsible for cooling in the Γ-valley. (i) While the Si-Si and the Ge-Ge bonds in hex-SiGe are assumed to be completely nonpolar, the randomly distributed Si-Ge bonds in the hex-SiGe alloy are still slightly polar. Although the random distribution of the Si-Ge bonds is expected to suppress the creation of large charge distributions, we cannot exclude a small amount of polar optical phonon emission by the Fröhlich interaction. (ii) Optical phonon emission by deformation potential scattering in the valence band might be a relatively strong process. Once the holes have cooled down, the electrons will also cool down by electron-hole scattering. (iii) Since the conduction band of hex-SiGe in the Γ-valley is of mixed s-type and p-type character, deformation potential scattering in the conduction band is also a possible and yet unknown carrier relaxation mechanism.

2. Experimental

Measurements of the carrier dynamics in Ge, GeSn or hex-SiGe are difficult due to the emission in the infrared[8,20,21]. We have measured the time-resolved photoluminescence spectra of hex-SiGe by combining a Fourier transform spectrometer and time-correlated single photon-counting. With this self-assembled combination, we reach a spectral resolution of 7 nm combined with a temporal resolutions of 22 ps. Together, they have the same potential as a streak camera, but now in the mid-infrared. This measurement is referred to as a time-resolved Fourier transform infrared (TR-FTIR) spectroscopy.

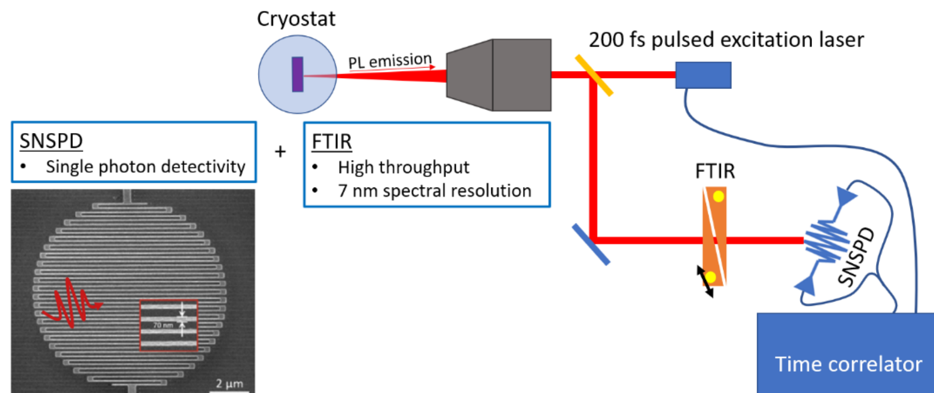

Figure 3: Schematic drawing of the TR-FTIR micro-photoluminescence set-up.

The set-up allows for excitation at 1032 nm (1.2 eV) with a NKT photonics Origami femtosecond laser with pulses of <200 fs at 40 MHz repetition rate. The excitation beam is focused using a Cassegrain reflective objective with a magnification of 32 (NA=0.38) resulting in an excitation spot size with a 3µm diameter at the sample inside the cryostat . The small spot-size allows for the excitation of one single nanowire. This setup is therefore referred to as micro-PL. The sample is mounted on a helium cooled cryostat and all measurements are performed at 4K lattice temperature. The emitted PL signal is collected by the same Cassegrain objective and split from the excitation beam using a beam splitter. The laser reflection is filtered from the PL emission using a 1350 nm (0.92 eV) long pass (LP) filter after which it is used as an input for the NIREOS Gemini Fourier transform interferometer (FTIR). The (interfering) signal from the FTIR module is in-coupled into an SM2000 single-mode fiber, transporting it for detection using time correlated single photon counting (TCSPC). The Single Quantum

superconducting nanowire single photon detector (SNSPD) has a ≳ 35% quantum efficiency at 1800 nm and ≳ 5% quantum efficiency at 2300 nm, 30 ns deadtime and 22 ps jitter. We use a PicoQuant PicoHarp TCSPC module with 4 ps time resolution to record the time between the emission of the laser pulse and the first arrival of a PL emitted photon at the SNSPD. Binning and counting the time delays of all detected photons results in a statistical measurement of the PL intensity decay over time, as shown in Fig. 4a. The unique combination of the FTIR module and TCSPC detector allows us to measure the PL decay time as a function of excess energy (Fig. 4b) as well as the time resolved PL spectra as a function time as shown in Fig. 4c. Altogether, the set-up covers a spectral window of 1350-2300 nm (0.54- 0.91 eV), determined by the cut-on of the LP filter and the drop in quantum efficiency of the SNSPD at long wavelengths. It provides a spectral resolution of 7 nm (limited by the FTIR module) and a time resolution of 22 ps (limited by the SNSPD).

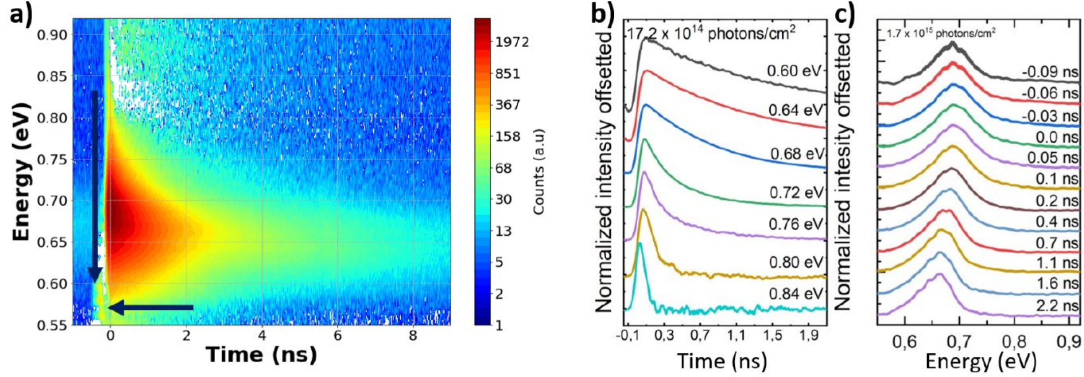

Figure 4: Example of a typical data set obtained by one TR-FTIR measurement. a) the 3D representation of intensity over time and energy. b) a stacked representation of cross sections of the date at different energies. The time domain represented is indicated by the vertical arrow in (a). c) a stacked representation of cross sections of the data at different times. The time domain represented is indicated by the horizontal arrow in (a).

In this research hex-SiGe nanowires (NWs) are investigated with two different alloy compositions. The compositions of interest are hex−$Si_{0.2}Ge_{0.8}$ and hex−$Si_{0.32}Ge_{0.68}$. Theoretically predicted energy values[19,22,23] of the conduction band minima of these two samples are displayed in Table I.

	$\mathrm{hex-Si_{0.2}Ge_{0.8}}$	$\mathrm{hex-Si_{0.32}Ge_{0.68}}$
Γ	0.55 eV	0.71 eV
M	0.75 eV	0.76 eV
U	0.66 eV	0.71 eV
L	0.80 eV	0.82 eV

Table I: Energy values of high symmetry points of hex−$Si_{0.2}Ge_{0.8}$ and hex−$Si_{0.32}Ge_{0.68}$.

The corresponding band structure representations are displayed in Fig. 5. These samples are of interest for carrier cooling investigation since they allow for the comparison of carrier cooling dynamics in an isolated Γ-valley band structure (hex−$Si_{0.2}Ge_{0.8}$, Fig. 5a) to carrier cooling dynamics in a band structure where the Γ-valley is surrounded by closely energy matched satellite valleys (hex−$Si_{0.32}Ge_{0.68}$, Fig. 5b). Both alloy compositions have experimentally proven to show direct band gap behavior[9]. Furthermore, the samples are selected to have their PL emission spectrum well within the spectral window of the micro-PL set up.

Sample	Core thickness (nm)	Shell thickness (μm)	NW length (μm)
$\mathrm{hex-Si_{0.2}Ge_{0.8}}$	120	2.4	9.2
$\mathrm{hex-Si_{0.32}Ge_{0.68}}$	180	1.3	8.4

Table II: Dimensions of the hex−$Si_{0.2}Ge_{0.8}$ and hex−$Si_{0.32}Ge_{0.68}$ nanowires with wurtzite GaAs cores and hex-SiGe shells, as measured using scanning electron microscopy. The growth is similar as described in the Fadaly paper[9].

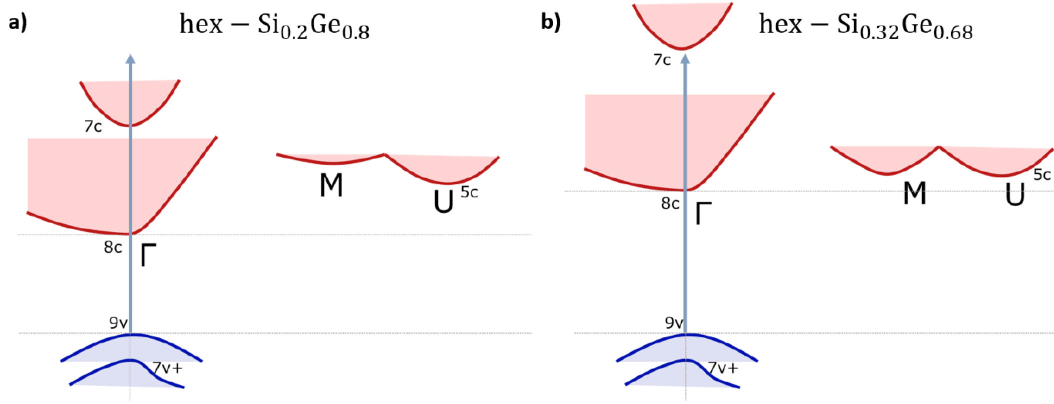

Figure 5: Schematic of band structure alignment of a hex−$Si_{0.2}Ge_{0.8}$ sample (a) and a hex−$Si_{0.32}Ge_{0.68}$ sample (b). Energy values of the band minima correspond to the values displayed in Table I. For reference, the excitation energy is displayed by the grey arrow.

Optical excitation with the 1.2eV laser source of the micro-PL setup, excites carriers far above the band gap energy for both alloy compositions. After excitation, the carriers have an excess energy of 0.65eV and 0.49eV for hex−$Si_{0.2}Ge_{0.8}$ and hex−$Si_{0.32}Ge_{0.68}$ respectively. The second conduction band minimum (Γ_{7c}) is located at 1.01eV and 1.23eV for hex−$Si_{0.2}Ge_{0.8}$ and hex−$Si_{0.32}Ge_{0.68}$, respectively[23]. This indicates that the excitation energy is sufficient to excite electrons into the second conduction band of hex−$Si_{0.2}Ge_{0.8}$ but not of hex−$Si_{0.32}Ge_{0.68}$.

We compare the carrier cooling dynamics in our hex-SiGe samples with those of a multiple-quantum well (MQW) InGaAs/InP sample, suitable for state-of-the-art quantum well-lasing applications. The InGaAs multiple quantum well consists of an the alternation of ~30nm InGaAs barrier layers and ~6nm InGaAs active layers emitting at 2 µm, nicely comparable to the hex-SiGe PL emission regime. Absorption can take place over the whole MQW structure as the excitation energy is above the band gap energy of the InGaAs buffer layers, resulting in a 625nm absorption thickness.
Recently, MQW structures have received a lot of attention because of the pronounced hot-phonon effects. It is not clear what exact mechanism(s) are by which the carrier cooling rate is suppressed. Hypothesis are confinement of the hot carrier movement, or localization of phonons emitted by the hot carriers[24–28].

3.1 Three dimensional maps of the carrier cooling dynamics in InGaAs MQWs and hex-SiGe

We first evaluate the operation of our setup by measuring time-resolved PL spectra from the InGaAs MQW sample at increasing excitation fluence, as shown in Fig. 6. This representation gives insight in both the spectral and time-resolved component of the PL emission. For the lowest fluence (0.004mJ/cm^2) (a), the PL spectral peak is narrow over the whole measured time domain. With increasing excitation fluence, a high-energy tail arises at t = 0, quickly narrowing down over time. This behavior is explained as the radiative recombination of hot carriers before they are fully relaxed to the bottom of the conduction band. The high energy tail can thus be interpreted as an indication of the hot carrier distribution. In other materials, these processes take place on a < 100ps timescale. The observation that the hot carriers become distinguishable indicates a reduction of hot carrier cooling due to hot phonon effects that can be particularly strong in multiple quantum wells materials[24–31].
In all graphs, high-intensity spikes at determined energies are visible. This is likely a result of an aliasing issue, due to an imperfect apodization on the sharp emission, resulting in fringe peaks on either side of the main peak. No further attention is devoted to this effect.

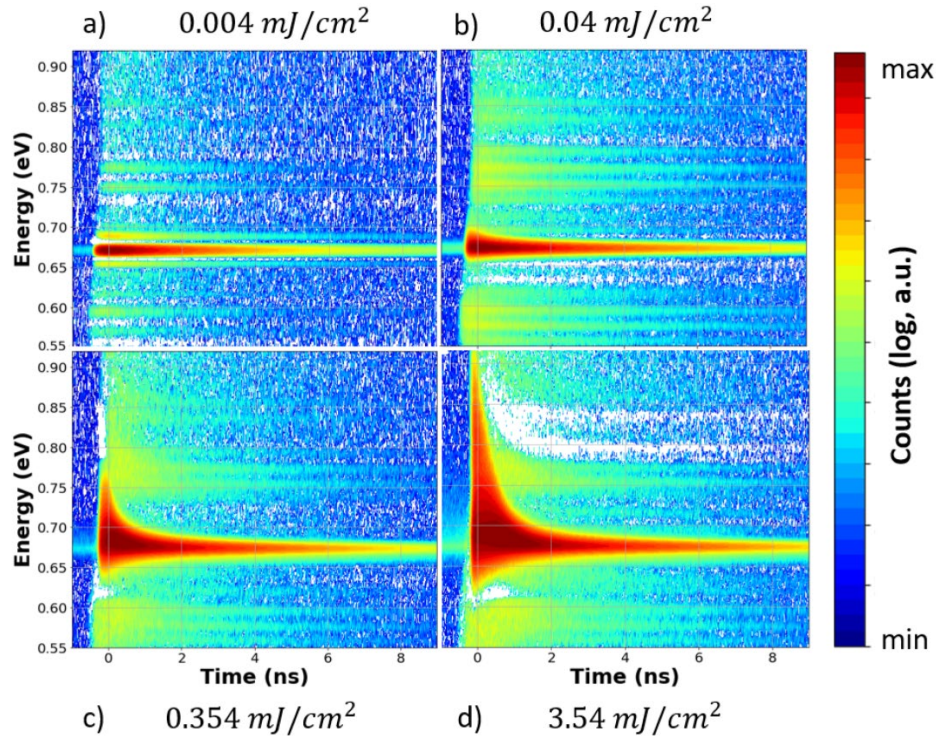

Figure 6: 3D representation of TR-FTIR measurements on the InGaAs MQW for increasing excitation fluence between 0.004mJ/cm² (a) and 3.54mJ/cm² (d). By increasing the excitation fluence, a high energy tail emission becomes apparent, indicating hot carriers in the material.

Fig. 7 represents a 3D visualizations of TR-FTIR measurements of the hex-SiGe samples, at 3.54mJ/cm² excitation. Comparable to the InGaAs MQW sample, the hex−$Si_{0.2}Ge_{0.8}$ sample (Fig. 7a) shows high energy tail emission, indicating the existence of hot carriers. In the hex−$Si_{0.32}Ge_{0.68}$ sample (Fig. 7b), the high energy tail is also present, although a bit less pronounced. Likely, the spectrum of the hex−$Si_{0.2}Ge_{0.8}$ sample is more symmetric than visualized in Fig. 7a. This is not observable due to the cut on of the filter used (at 0.55eV), altering the spectral shape at the low energy side. The high-energy side of the spectrum remains unaltered by this effect. Since hot carrier cooling is visible in the high-energy tail of the spectrum, this is not a major problem for the research presented here.

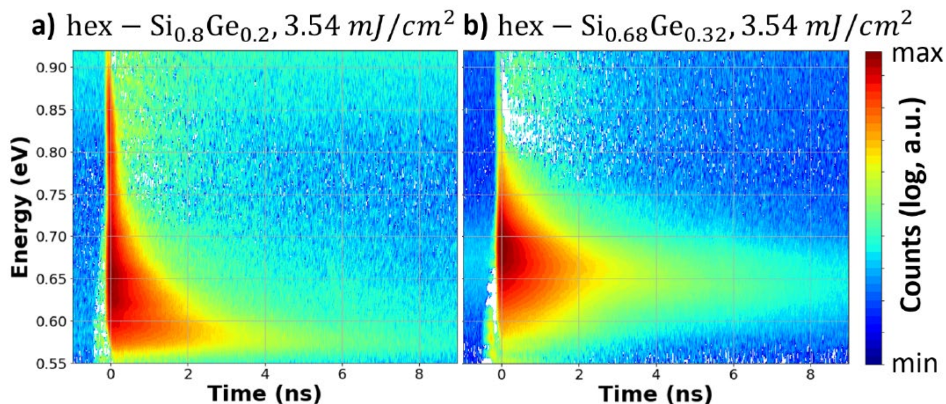

Figure 7: 3D representation of TR-FTIR measurements on the hex−$Si_{0.2}Ge_{0.8}$ (a) and hex−$Si_{0.32}Ge_{0.68}$ b) sample after excitation with a laser fluence of 3.54mJ/cm². The presence of high energy tail emission, comparable to the high fluence InGaAs MQW measurements in Fig. 6, indicates the existence of hot carriers in the system.

3.2 Carrier cooling dynamics as a function of time

Fig. 8a shows the evolution of the PL emission spectrum for hex−$Si_{0.2}Ge_{0.8}$ at 3.54mJ/cm^2 excitation, as obtained from the TR-FTIR datasets shown in Fig. 7. The displayed time intervals are chosen on a logarithmic scale since most interesting behavior takes place at short time scales. At short time delays, a high energy emission tail is observed, which can be described by a Fermi Dirac distribution. This tail becomes steeper over time (indicated by a yellow arrow). This can be attributed to hot carrier cooling as a function time.

We fit the time-resolved photoluminescence spectra $j_\gamma(\hbar\omega)$ by Planck's black-body radiation law which has been generalized by both Lasher and Stern[32] and also by Würfel[33] by

$$j_\gamma(\hbar\omega) = \frac{(\hbar\omega)^2}{4\pi^2\hbar^3c^2}\frac{a(\hbar\omega)}{exp\left(\frac{\hbar\omega-\Delta\mu}{k_BT}\right)-1}, \quad (1)$$

where $a(\hbar\omega)$ is the absorptivity which is defined in terms of its absorption coefficient $\alpha(\hbar\omega)$ by

$$a(\hbar\omega) = (1-R)\left[1-e^{-\alpha(\hbar\omega)d}\right], \quad (2)$$

with R the reflectivity and d the absorption length. This Lasher-Stern-Würfel (LSW) equation shows that in quasi-equilibrium, the band-to-band recombination is fully described by the quasi-Fermi level splitting $\Delta\mu$. If we subsequently introduce the absorption coefficient $\alpha(\hbar\omega)$ as being a product of the joint density of states function near the bandgap, which is described by $\sqrt{\hbar\omega - E_g}$, multiplied by an occupation correction factor $[f_l - f_u]$ and broadened by an Urbach tail that can be described by $N(\gamma,\theta)exp\left(-\left|\frac{\hbar\omega}{\gamma}\right|^\theta\right)$ the resulting photoluminescence spectrum can be written as

$$j_\gamma(\hbar\omega) = \frac{(\hbar\omega)^2 a(\hbar\omega)}{exp\left(\frac{\hbar\omega-\Delta\mu}{k_BT}\right)-1} \times \left[N(\gamma,\theta)exp\left(-\left|\frac{\hbar\omega}{\gamma}\right|^\theta\right) \times \sqrt{\hbar\omega - E_g}\right] \times [f_l(\varepsilon_l,\mu_h) - f_u(\varepsilon_u,\mu_e)] \quad (3)$$

in which the constants are given by Katahara[34]. The LSW fit is applied on the spectra from the 80% max-intensity point on the low-energy side of the spectrum, until the cut-on of the filter (at 0.92 eV). Lower energies < 80% intensity are not taken into account in order to prevent large contributions of variation in the fiber efficiency and detector cutoff. Furthermore, it prevents contributions of a possible Urbach tail, which is not taken into account in the fit function. The dashed lines in Fig. 8a represent the LSW fits applied to the data.

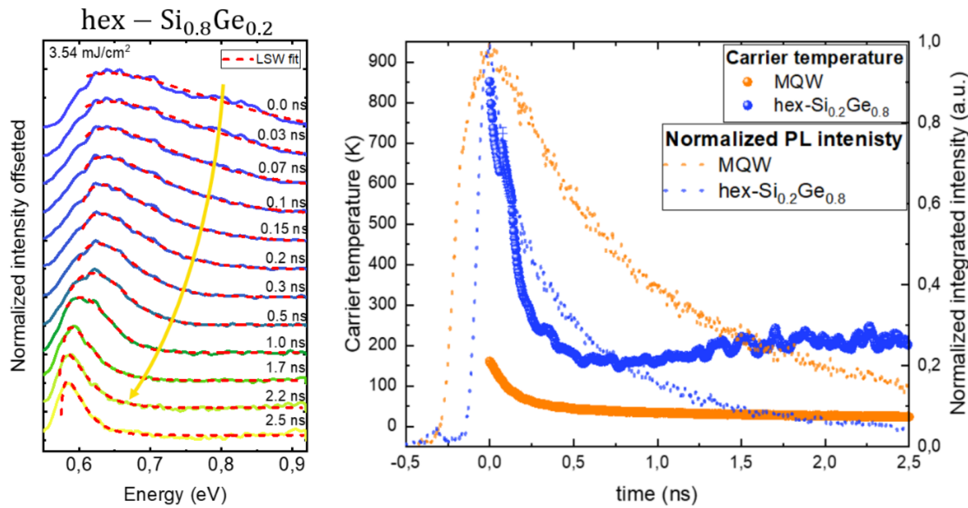

Figure 8: (a) PL emission spectrum over time of the hex−$Si_{0.2}Ge_{0.8}$. The arrow indicates the effect of cooling of the carrier temperature over time. The dashed lines represent the Lasher Stern Wurfel fit. (b) Fitted carrier temperature as a function of time in both hex−$Si_{0.2}Ge_{0.8}$ (blue) and the InGaAs MQW (orange), together with the integrated PL intensity as a function of time.

Application of the LSW fits on all spectra over time, provides us with the evolution of the carrier temperature as a function of time, or the energy loss rate[35], in Fig. 8b. The dotted lines represent the integrated PL emission intensity over time. For both samples, a clear decrease in the carrier temperature can be observed over time. The carrier temperature in hex−$Si_{0.2}Ge_{0.8}$ (blue) starts at an initial temperature of ~ 851K and cools down to a temperature of ~ 160K. The InGaAs MQW (orange) starts at an initial temperature of ~200K, relaxing to a temperature of ~ 24K, which is approximately the initial lattice temperature (~10K). The behavior of the carrier temperature over time will be extensively discussed later. For now, we first look at the other parameters we obtained from the model.

3.3 Alloy composition dependence of the cooling dynamics

A comparison of the evolution of the carrier temperature over time for the two hex-SiGe compositions is displayed in Fig. 9a. There is a large difference of ~ 500K, in initial carrier temperature between both samples becomes visible (as indicated by the red-dashed line). We attribute this difference to the different electronic band structures of the two alloy ratios as displayed in Fig. 9b.

In hex−$Si_{0.32}Ge_{0.68}$, similar to cubic-Ge, intervalley scattering allows for cooling almost to the bottom of the Γ-valley in the conduction band. This causes the carriers to relax to low temperatures (200-300K) in a short time (< 100fs). This relaxation is not visible in our measurements due to the limited temporal resolution of our setup.

As introduced before, the isolated Γ valley of hex−$Si_{0.2}Ge_{0.8}$ is expected to limit the contribution of intervalley scattering. This causes the initially observed carrier temperature to be as high as 800K. The observation of an alloy-ratio dependent initial carrier temperature supports the hypothesis of a reduced contribution of intervalley scattering to the carrier relaxation dynamics in hex−$Si_{0.2}Ge_{0.8}$, featuring an isolated Γ-valley. The observed difference in initial temperature between hex−$Si_{0.2}Ge_{0.8}$ and hex−$Si_{0.32}Ge_{0.68}$ value of 500 K translates to an energy of ~0.04eV. This energy is comparable to the expected difference in energy minima of the U-valleys of hex−$Si_{0.2}Ge_{0.8}$ and hex−$Si_{0.32}Ge_{0.68}$ of ~0.05eV as introduced in Table I. It must however be noted that the fitted carrier temperature describes the temperature of a distribution of carriers. It can therefore not be one-to-one related to one-carrier energy transitions in an electronic band structure. This result should therefore be interpreted as a qualitative trend rather than a quantitative measurement.

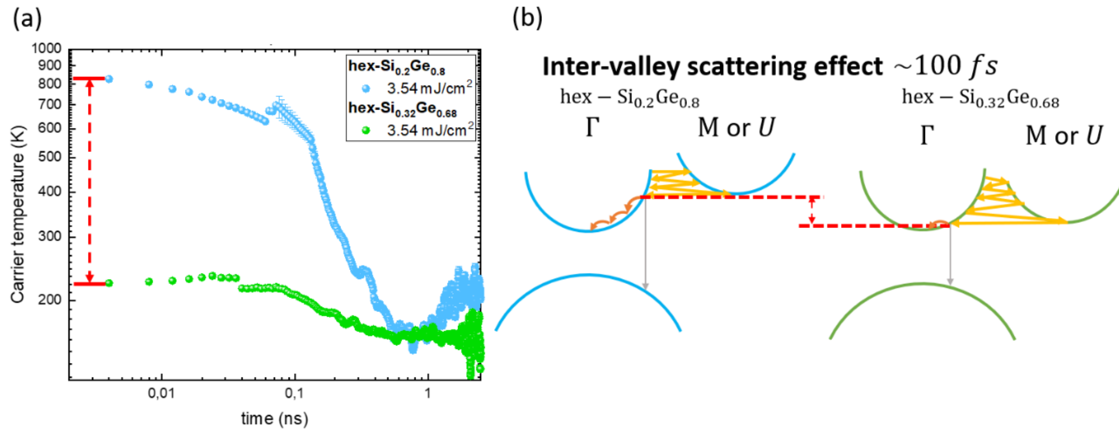

Figure 9: Comparison of the measured carrier temperature for the two different alloy compositions (hex−$Si_{0.2}Ge_{0.8}$ (blue) and hex−$Si_{0.32}Ge_{0.68}$ (green)). The large difference in initial carrier temperature, as indicated with the red-dashed arrow, is explained by the different contributions of the very fast intervalley scattering to the slower hot carrier cooling, as schematically represented in (b).

3.4 Influence of hot-phonon effects on the cooling dynamics in hex-SiGe

Fitted energy loss rates for different excitation fluences are displayed in Fig. 10. In the InGaAs MQW (a), with increasing excitation fluence, a higher initial carrier temperature and slower cooling are

observed (indicated by the red-dashed arrow). This can be explained by carrier-LO phonon relaxation creating hot phonons which are in turn heating up the carriers. Hot phonon effects are particularly important when the carrier-LO phonon scattering rate approaches the hot phonon relaxation rate in which an optical phonon is e.g. converted into 2 longitudinal acoustic phonons by the Klemens process[25,26]. The presence of non-equilibrium phonons results in a reduction of the carrier cooling process.
In the hex−$Si_{0.2}Ge_{0.8}$ and hex−$Si_{0.32}Ge_{0.68}$ samples, a different trend is observed. The carrier cooling time seems to be much less determined by the excitation fluence, thus suggesting that hot phonon effects are less important in hex-SiGe. This results might be partly understood by the fact that the initial cooling from the laser energy at 1.2 eV to the bottom of the M and U bands is governed by zone-edge phonons instead of the small q phonons responsible for the Fröhlich interaction in a III/V semiconductor. A second reason might be the expected non-existent phonon band gap in Group IV semiconductors, reducing the non-equilibrium phonon effects.

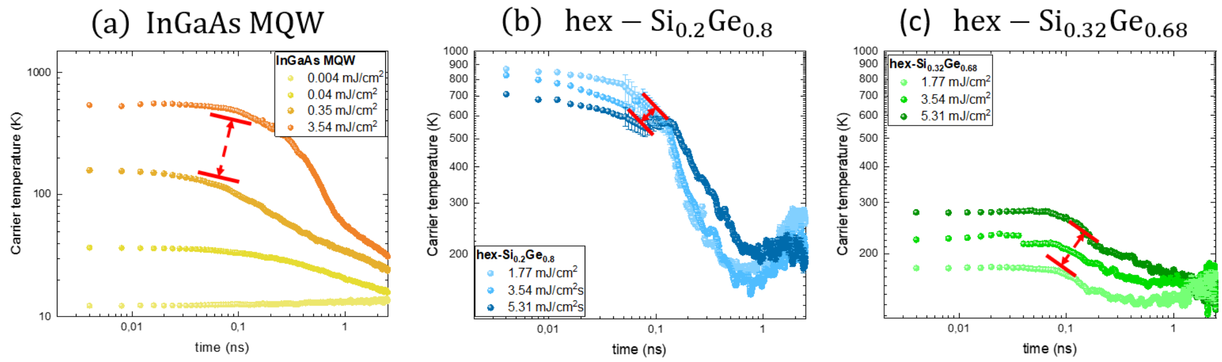

Figure 10: Carrier temperature relaxation as a function of time after excitation with different laser fluences. Both the temperature and time are displayed on a log scale providing better insight into exponential processes. The results obtained from the InGaAs MQW (a), shows a strong reduction of the carrier cooling rate with increasing fluence, pointing towards non-equilibrium phonon effects. The results of the hex−$Si_{0.2}Ge_{0.8}$ (b) and the hex−$Si_{0.32}Ge_{0.68}$ sample (c), suggest a small effect of non-equilibrium phonon effects, however a lot less pronounced compared to the InGaAs MQW sample. It is important the note the difference in y-axis between (a) and (b) & (c), hiding the saturation of hot carrier cooling at high temperatures in hex-SiGe.

3.5 Electron-phonon scattering time in hex-SiGe

In both Figs. 9 and 10, hot-carrier cooling of hex-SiGe seems to saturate at high temperatures (~200K). This effect is especially clear in comparison to the InGaAs MQW measurements which cool down to approximately lattice temperature set by the cryostat. Although, reduced carrier cooling rates are more often observed[37], a saturation at ~200K, whilst the lattice is assumed to be at ~10K, is an order of magnitude above all reported values plateau values. In this report, we will focus to the dominant carrier cooling regime between below ~0.6 ns. We presently do not yet understand the plateau values which might be due to lattice heating[37] or trapping of carriers.

A simplified model for the carrier cooling rates was introduced by Shah[38,39]. This model was initially derived for Group III-V semiconductors. Since in Group III-V semiconductors the Fröhlich assisted electron-LO phonon scattering is the dominant carrier cooling mechanism. As introduced before, electron-LO phonon scattering is efficient when $k_B T_{carrier} > \hbar\omega_{LO}$ and quickly reduces in efficiency when $k_B T_{carrier} < \hbar\omega_{LO}$. Taking this energy dependence into account, a differential equation for the energy decay over time is described as

$$\langle \frac{dE}{dt} \rangle = \frac{C\hbar\omega_{LO}}{\tau_{LO}} e^{\frac{-\hbar\omega_{LO}}{k_B T}} \tag{4}$$

with τ_{LO} being the electron-LO phonon scattering time and $\hbar\omega_{LO}$ the LO-phonon energy. *C* is an empirical scaling parameter that accounts for the scattering ideality. *C* = 1 indicates ideal scattering and *C* = 0, indicates nonexistent scattering. For example, the reduction of the carrier-LO phonon interaction by the existence of non-equilibrium phonons has often been incorporated in the C value []. Eq. 4 can be easily converted into an equation that directly described the carrier cooling in terms of the carrier temperature $T_{carrier}$ by

$$\langle\frac{dT_{carrier}}{dt}\rangle = \frac{2C\hbar\omega_{LO}}{3k_B\tau_{LO}} e^{\frac{-\hbar\omega_{LO}}{k_B T_{carrier}}}. \quad (5)$$

We fit the carrier cooling curves in Fig. 11 with the model as described by Eq. 5. The energy of the LO phonon is used as a fitting parameter in order to take into account the energy dependence of carrier-LO phonon scattering rate. As Eq. 5 is originally formulated for the Fröhlich interaction between carriers and LO-phonons, one phonon mode was assumed to be dominant in the material. This mode can then be described by one LO-phonon energy ($\hbar\omega_{LO}$). In our case, due to the alloy nature of both hex-SiGe and the reference InGaAs MQW, we have to determine the average LO-phonon energy in the material. As introduced before, the phonon population in a material can be measured using Raman spectroscopy. In order to determine the LO-phonon energies for hex-SiGe, we rely on the Raman spectroscopy measurements of De Matteis et al.[40]. From their calculations we predict an average LO-phonon energy of 39.46meV and 42.42meV for the hex−$Si_{0.2}Ge_{0.8}$ and hex−$Si_{0.32}Ge_{0.68}$ alloy composition. For the InGaAs MQW, we use an average LO-phonon energy of 33meV, determined for a comparable InGaAs MQW structure by Zou et al.[41]. These values are used as input for the $\hbar\omega_{LO}$ parameter in Eq. 5.When using Eq. 5 as a fitting function, the interdependent nature of the scattering rate (τ_{LO}) becomes apparent. In order to make the fit converge, it is decided to set C to 1. With that we determine a maximum value for τ_{LO}, referred to as the effective carrier-LO phonon scattering time (τ_{LO}). This value incorporates both the carrier-LO phonon scattering time and the physical phenomena determining the value of C as explained above.

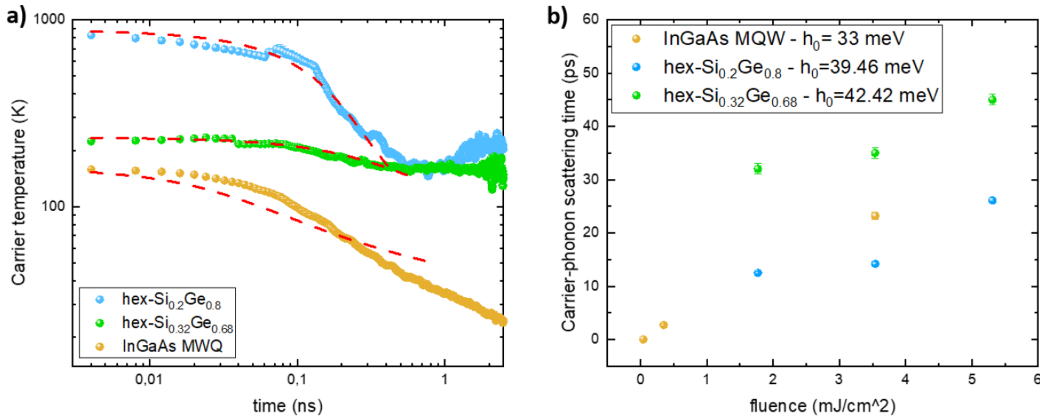

*Figure 11:(a) Obtained carrier temperatures from Figs 6,7, fitted by the carrier cooling curve (*Eq. 5*). (b) Graph of effective τ_{LO} as a function of excitation fluence, with the used values for $h_0 = \hbar\omega_{LO}$.*

Fluence (mJ/cm^2)	InGaAs MQW $\hbar\omega_{LO}$= 33meV	hex−$Si_{0.2}Ge_{0.8}$ $\hbar\omega_{LO}$ = 39.46 meV	hex−$Si_{0.32}Ge_{0.68}$ $\hbar\omega_{LO}$ = 42.42 meV
0.35	2.7 ±0.3ps		
1.76		12.5 ±0.3ps	32 ±1ps
3.53	23.2 ±0.7ps	14.2 ±0.4ps	35 ±1ps
5.30		26.1 ±0.5ps	45 ±1ps

Table III: Effective carrier-LO phonon scattering times (τ_{LO}).

3.6 Comparison of hex-SiGe and InGaAs MQWs for laser applications

We found that the carrier relaxation in InGaAs MQWs are strongly limited by hot phonon effects while the carrier relaxation in hex-SiGe is limited by deformation potential scattering in the isolated Γ-valley. The mechanisms which determine the carrier cooling dynamics in InGaAs multiple quantum wells and in hex-SiGe are thus quite different. Nevertheless, Fig. 12 shows that the hot carrier lifetimes of hex-SiGe are quite comparable to the InGaAs MQW sample at normal threshold laser fluence excitation.

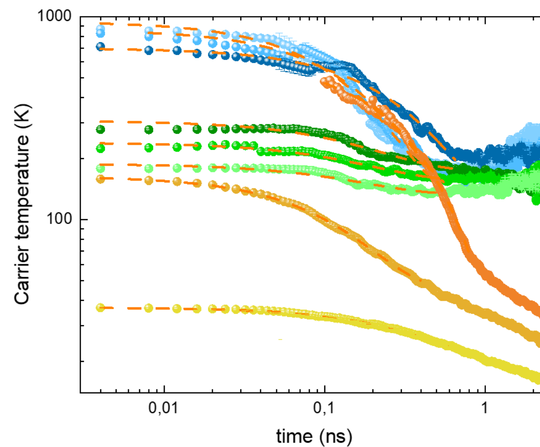

Figure 12: Carrier cooling for hex−$Si_{0.2}Ge_{0.8}$ in blue, hex−$Si_{0.32}Ge_{0.68}$ in green and the InGaAs MQW in orange. The excitation densities are 1.76 mJ/cm^2, 3.53 mJ/cm^2, and 5.30 mJ/cm^2 for both the hex-SiGe samples and 0.04 mJ/cm^2, 0.35 mJ/cm^2, and 3.54 mJ/cm^2 for the InGaAs MQW.

In conclusion, the hot-carrier lifetimes in hex-SiGe are found to be comparable to the InGaAs MQW after excitation laser fluences required for normal threshold lasers. The absence of the Fröhlich interaction is therefore not expected to limit the lasing capabilities of hex-SiGe. Further research is required to increase quantitative understanding of the strength of the different cooling mechanisms in hex-SiGe.

References

1. Armand Pilon, F. T. *et al.* Lasing in strained germanium microbridges. *Nature Communications* **10**, 6–13 (2019).
2. Wirths, S. *et al.* Lasing in direct-bandgap GeSn alloy grown on Si. *Nature Photonics* **9**, 88–92 (2015).
3. Soref, R., Buca, D. & Yu, S.-Q. Group IV Photonics: Driving Integrated Optoelectronics. *Optics and Photonics News* **27**, 32 (2016).
4. Elbaz, A. *et al.* Ultra-low-threshold continuous-wave and pulsed lasing in tensile-strained GeSn alloys. *Nature Photonics* **14**, 375–382 (2020).
5. Amoah, S. *et al.* Electrically Injected GeSn Laser on Si Operating up to 110K. *2021 Conference on Lasers and Electro-Optics, CLEO 2021 - Proceedings* **7**, (2021).
6. Buca, D. *et al.* Room Temperature Lasing in GeSn Microdisks Enabled by Strain Engineering. *Advanced Optical Materials* **10**, (2022).
7. Stange, D. *et al.* GeSn/SiGeSn Heterostructure and Multi Quantum Well Lasers. *ACS Photonics* **5**, 4628–4636 (2018).
8. Rogowicz, E. *et al.* Carrier Dynamics in Thin Germanium-Tin Epilayers. *ACS Applied Electronic Materials* **3**, 344–352 (2021).
9. E.M.T. Fadaly et al. Direct Band Gap Emission from Hexagonal Ge and SiGe Alloys. *Nature* **580**, 205–209 (2020).

10. Ciano, C. *et al.* Electron-phonon coupling in n -type Ge two-dimensional systems. *Physical Review B* **102**, 1–8 (2020).
11. Lange, C. *et al.* Comparison of ultrafast carrier thermalization in Gax In1-x As and Ge quantum wells. *Physical Review B - Condensed Matter and Materials Physics* **81**, 1–6 (2010).
12. Sjakste, J., Tanimura, K., Barbarino, G., Perfetti, L. & Vast, N. Hot electron relaxation dynamics in semiconductors: Assessing the strength of the electron-phonon coupling from the theoretical and experimental viewpoints. *Journal of Physics Condensed Matter* **30**, 353001 (2018).
13. Pezzoli, F. *et al.* Spin and energy relaxation in germanium studied by spin-polarized direct-gap photoluminescence. *Physical Review B - Condensed Matter and Materials Physics* **88**, 1–12 (2013).
14. Tanaka, K., Ohtake, H. & Suemoto, T. Determination of Intervalley Scattering Time in Germanium by Subpicosecond Time-Resolved Raman Spectroscopy Koichiro. *Phys.Rev.Lett.* **71**, 1935–38 (1993).
15. Mak, G. & Rühle, W. W. Femtosecond carrier dynamics in Ge measured by a luminescence up-conversion technique and near-band-edge infrared excitation. *Physical Review B* **52**, 584–587 (1995).
16. Zürch, M. *et al.* Direct and simultaneous observation of ultrafast electron and hole dynamics in germanium. *Nature Communications* **8**, (2017).
17. Roskos, H., Rieck, B., Seilmeier, A. & Kaiser, W. Cooling of a carrier plasma in germanium investigated with subpicosecond infrared pulses. *Applied Physics Letters* **53**, 2406–2408 (1988).
18. Cardona, M. & Yu, P. Y. *Fundamentals of Semiconductors: Physics and Materials Properties, 4th Edition*. (Springer Cham Heidelberg New York Dordrecht London, 2010).
19. Rödl, C. *et al.* Accurate electronic and optical properties of hexagonal germanium for optoelectronic applications. *Phys.Rev.Materials* **3**, 034602 (2019).
20. Julsgaard, B. *et al.* Carrier lifetime of GeSn measured by spectrally resolved picosecond photoluminescence spectroscopy. *Photonics Research* **8**, 788 (2020).
21. Huang, P. *et al.* Study of ultrafast carrier dynamics in GeSn thin film by time-resolved terahertz spectroscopy. *Chinese Physics B* (2023) doi:10.1088/1674-1056/accf7f.
22. Suckert, J. R., Rödl, C., Furthmüller, J., Bechstedt, F. & Botti, S. PHYSICAL REVIEW MATERIALS 5 , 024602 (2021) Efficient strain-induced light emission in lonsdaleite germanium. **024602**, 1–9 (2021).
23. Borlido, P. *et al.* From pseudo-direct hexagonal germanium to direct silicon-germanium alloys. *Physical Review Materials* **5**, 1–5 (2021).
24. Conibeer, G., Zhang, Y., Bremner, S. P. & Shrestha, S. Towards an understanding of hot carrier cooling mechanisms in multiple quantum wells. *Japanese Journal of Applied Physics* **56**, (2017).
25. Ferry, D. K. Non-equilibrium longitudinal optical phonons and their lifetimes. *Applied Physics Reviews* **8**, (2021).
26. Zhang, Y., Conibeer, G., Liu, S., Zhang, J. & Guillemoles, J. F. Review of the mechanisms for the phonon bottleneck effect in III–V semiconductors and their application for efficient hot carrier solar cells. *Progress in Photovoltaics: Research and Applications* **30**, 581–596 (2022).
27. Conibeer, G. *et al.* Hot carrier solar cell absorber prerequisites and candidate material systems. *Solar Energy Materials and Solar Cells* **135**, 124–129 (2015).
28. Harada, Y., Kasamatsu, N., Watanabe, D. & Kita, T. Nanosecond-scale hot-carrier cooling dynamics in one-dimensional quantum dot superlattices. *Physical Review B* **93**, 1–5 (2016).
29. Zhou, Y. *et al.* Electrically injected GeSn lasers with peak wavelength up to 2.7 µm. *Photonics Research* **10**, 222 (2022).
30. Sadasivam, S., Chan, M. K. Y. & Darancet, P. Theory of Thermal Relaxation of Electrons in Semiconductors. *Physical Review Letters* **119**, 1–6 (2017).
31. Shojaei, I. A. *et al.* Strong Hot Carrier Effects in Single Nanowire Heterostructures. *Nano Letters* **19**, 5062–5069 (2019).
32. Lasher, G., Stern, F. & G. Lasher and F. Stern. Spontaneous and stimulated recombination radiation in semiconductors. *Phys. Rev.* **133**, A553 (1964).

33. P.Würfel. The chemical potential of radiation. *Journal of Physics C: Solid State Physics* **15**, 3967–3985 (1982).
34. Katahara, J. K. & Hillhouse, H. W. Quasi-fermi level splitting and sub-bandgap absorptivity from semiconductor photoluminescence. *Journal of Applied Physics* **116**, 173504 (2014).
35. Shah, J., Pinczuk, A., Gossard, A. C. & Wiegmann, W. Energy-loss rates for hot electrons and holes in GaAs quantum wells. *Physical Review Letters* **54**, 2045–2048 (1985).
36. Barman, S. & Srivastava, G. P. Long-wavelength nonequilibrium optical phonon dynamics in cubic and hexagonal semiconductors. *Physical Review B - Condensed Matter and Materials Physics* **69**, 235208 (2004).
37. Tedeschi, D. *et al.* Long-Lived Hot Carriers in III-V Nanowires. *Nano Letters* **16**, 3085–3093 (2016).
38. Shah, J. Hot Carriers in Quasi-2-D Polar Semiconductors. *IEEE Journal of Quantum Electronics* **22**, 1728–1743 (1986).
39. Shah, J. *Ultrafast Spectroscopy of Semiconductors and Semiconductor Nanostructures*. (Gmbh, Springer-verlag Berlin Heidelberg, 1999). doi:10.1007/978-3-662-03770-6.
40. De Matteis, D. *et al.* Probing Lattice Dynamics and Electronic Resonances in Hexagonal Ge and SixGe1- xAlloys in Nanowires by Raman Spectroscopy. *ACS Nano* **14**, 6845–6856 (2020).
41. Zou, Y., Esmaielpour, H., Suchet, D., Guillemoles, J. F. & Goodnick, S. M. The role of nonequilibrium LO phonons, Pauli exclusion, and intervalley pathways on the relaxation of hot carriers in InGaAs/InGaAsP multi-quantum-wells. *Scientific Reports* **13**, 1–13 (2023).